RESEARCH ARTICLE

Numerical study of transient evolution of lifted jet flames: partially premixed flame propagation and influence of physical dimensions

Zhi Chen*, Shaohong Ruan and Nedunchezhian Swaminathan

Department of Engineering, Cambridge University, Cambridge CB2 1PZ, UK

Three-dimensional (3D) unsteady RANS simulations of a spark-ignited turbulent methane/air jet flame evolving from ignition to stabilisation are conducted for different jet velocities. A partially premixed combustion model is used involving a correlated joint Probability Density Function (PDF) and both premixed and non-premixed combustion mode contributions. The 3D simulation results for the temporal evolution of flame leading edge are compared with previous 2D results and experimental data. The comparison shows that the final stabilised flame lift-off height is well predicted by both 2D and 3D computations. However, the transient flame leading edge evolution computed from 3D simulation agrees reasonably well with the experiment, whereas evident discrepancies were found in the previous 2D study. This difference suggests that the third physical dimension plays an important role during the flame transient evolution process. The flame brush leading edge displacement speed resulting from reaction, normal and tangential diffusion processes are studied at different typical stages after ignition to further understand the effect of the third physical dimension. Substantial differences are found for the reaction and normal diffusion components between 2D and 3D simulations especially in the initial propagation stage. The evolution of reaction progress variable scalar gradients and its interaction with the flow and mixing field in the 3D physical space have an important effect on the flame leading edge propagation.

Keywords: partially premixed combustion; flame lift-off height; physical dimension influence; edge flame propagation; flame displacement speed

1.   Introduction

Flame propagation exists in various practical combustion systems involving the transition from a cold mixing to a stable burning state. This process is crucial for devices such as IC engines and aero gas turbines because of its important role in flame stabilisation, combustion instability and pollutant emissions, etc. In these practical applications, the flame often propagates in an unevenly premixed mixture of fuel and oxidiser involving many complex physical processes interacting with one another, which therefore introduce considerable modelling challenges [1].

Turbulent lifted jet flames have received much of the attention due to its simple geometry and richness in physics, especially at the flame base region where the reactants are partially premixed experiencing a high scalar dissipation rate. Many experimental and numerical studies have been conducted on these flames as reviewed in [2–4]. There are many complex physical processes, such as premixed flame propagation, non-premixed flamelets extinction, triple flames, large-scale structures, involved in the flame stabilisation as summarised in [5, 6]. These effects are considered in modelling works involving premixed [7]

---

*Corresponding author. Email: zc252@cam.ac.uk

and non-premixed [8] flamelets, G-equation (level-set approach) [9] and Conditional Moment Closure [10]. Although computed lift-off heights compared well with experimental data in these calculations, the lift-off height evolution and transient flame propagation characteristics are seldom addressed.

Amongst these transient characteristics, the flame displacement speed, S_d, defined as the flame propagation speed relative to the flow velocity [1, 11] is particularly of research interest. Displacement speed has been extensively studied for turbulent premixed flames using scaling analysis, direct numerical simulation (DNS), large eddy simulation (LES) and Reynolds-averaged Naiver-Stokes (RANS) methods as reviewed in [1, 12, 13]. However, the displacement speed behaviour in partially premixed mixture is not fully understood yet. A few two-dimensional (2D) DNS studies have investigated laminar triple or *tribrachial* flames propagation [14, 15] and edge flame velocity in the event of turbulent diffusion flame extinction [16]. These studies have shown that both premixed and non-premixed combustion modes contribute to the flame edge propagation and their contributions vary in the flame structure depending on the local mixing conditions. Furthermore, Im and Chen [14] found that the correlation between displacement speed and scalar dissipation rate can be positive or negative. More recently, Chakraborty and Mastorakos [17] conducted a further three-dimentional (3D) DNS study on edge flame propagation in turbulent mixing layers and the results show similar behaviours as observed in laminar flame simulations. However, the behaviours of displacement speed, both overall and its components from reaction, normal and tangential diffusion [17], are observed to be nonmonotonic with mixture fraction gradient. These complexities further increase the modelling challenge for flames propagating in turbulent partially premixed mixtures.

The 2D URANS study of Müller *et al.* [9], extended G-equation approach for partially premixed combustion involving a turbulent burning velocity, $S_{T,p}$, to capture the lift-off height and its temporal variation. The $S_{T,p}$ model included three terms accounting for premixed flame propagation, partial premixing and flamelet quenching respectively, and showed a quite good agreement with experimental data, despite a large scatter (uncertainty over 50%) in the measured values. They have also shown that the premixed flame propagation term dominates in the initial stage of propagation, whereas the flamelet quenching term controls the final lift-off height as the flame approaches the stabilisation region. Large-eddy simulation (LES) of the lifted flame ignited at downstream using a thickened flame model showed a good agreement between measured and computed transient evolution of the leading edge [18]. Satisfactory comparisons were also obtained by Jones and Prasad [19] using an LES-pdf approach with Eulerian stochastic fields. In the present study, the partially premixed combustion modelling framework developed by Ruan *et al.* [5] is used to investigate the transient evolution of the lift-off height using unsteady Reynolds averaged Navier-Stokes (URANS) approach. This combustion submodel has shown good capabilites to predict the final lift-off height in 2D steady RANS simulations of hydrogen [5] and methane [6] flames under various jet velocity and fuel dilution conditions. The 2D URANS simulations performed in [6] showed a considerable deviation between computed and measured [20] transient evolution of the most leading edge from ignition to final stabilisation despite the final lift-off height compared very well with measured values. It has been suggested in [6] that this difference could result from the use of axisymmetric configuration restricting the evolution of scalar and its gradient fields to 2D leading to substantial difference in the propagation speed of the flame brush leading edge as it evolves towards its final lift-off height. The influence of the physical dimension on the leading edge displacement speed was not studied. Hence it is worthwhile to address this before embarking on LES studies using the partially premixed combustion modelling used in [5] and [6].

The objective of this paper is to conduct 3D URANS simulations and to compare its results with previous 2D results in [6] to address the influence of physical dimension

on the lift-off height transient evolution. This is achieved by analysing the displacement speeds (both reactive and diffusive components [1]) of the flame brush leading edge at various stages of flame brush evolution in 2D and 3D simulations.

This paper is organised as follows. The modelling methodology is briefly presented in Section 2 as elaborate details are available in [5, 6]. The experiments considered for this study are described in Section 3, followed by the description of computational setup in Section 4. The results are discussed in Section 5 and the conclusions are summarised in the final section.

2.   Modelling methodology

2.1   *Governing Equations*

In addition to the Favre-averaged equations for continuity, momentum and total (sensible + chemical) enthalpy, five scalar transport equations are solved. These scalars are the first two moments of mixture fraction, $\widetilde{Z}$ and $\widetilde{Z''^2}$, and a reaction progress variable, $\widetilde{c}$ and $\widetilde{c''^2}$, as well as the covariance, $\widetilde{Z''c''}$, characterising the statistical dependence between Z and c. These additional equations are written using common notations as

$$\bar{\rho}\,\mathcal{D}_t\widetilde{Z} = \nabla \cdot \left(\overline{\rho D \nabla Z} - \overline{\rho u''Z''}\right), \tag{1}$$

$$\bar{\rho}\,\mathcal{D}_t\widetilde{Z''^2} = \nabla \cdot \left(\overline{\rho D \nabla Z''^2} - \overline{\rho u''Z''^2}\right) - 2\bar{\rho}\widetilde{\chi}_Z - 2\overline{\rho u''Z''} \cdot \nabla\widetilde{Z}, \tag{2}$$

$$\bar{\rho}\,\mathcal{D}_t\widetilde{c} = \nabla \cdot \left(\overline{\rho D \nabla c} - \overline{\rho u''c''}\right) + \overline{\dot{\omega}_c^*}, \tag{3}$$

$$\bar{\rho}\,\mathcal{D}_t\widetilde{c''^2} = \nabla \cdot \left(\overline{\rho D \nabla c''^2} - \overline{\rho u''c''^2}\right) - 2\bar{\rho}\widetilde{\chi}_c - 2\overline{\rho u''c''} \cdot \nabla\widetilde{c} + 2\overline{c''\dot{\omega}_c^{*''}}, \tag{4}$$

and

$$\bar{\rho}\,\mathcal{D}_t\widetilde{Z''c''} = \nabla \cdot \left(\overline{\rho D \nabla Z''c''} - \overline{\rho u''Z''c''}\right) - 2\bar{\rho}\widetilde{\chi}_{Zc} - 2\overline{\rho u''c''} \cdot \nabla\widetilde{Z} + \overline{\rho u''Z''} \cdot \nabla\widetilde{c} + 2\overline{Z''\dot{\omega}_c^{*''}}, \tag{5}$$

where $\mathcal{D}_t \equiv \partial_t + \widetilde{U} \cdot \nabla$ is the substantial derivative and D is the molecular diffusivity. The turbulent scalar fluxes are modelled using the gradient transport approximation following [5] and [6]. The Favre-averaged scalar dissipation rate of mixture fraction fluctuation and cross dissipation rate, $\widetilde{\chi}_Z$ and $\widetilde{\chi}_{Zc}$, are modelled using a turbulence time scale [5, 6], $t_f = \widetilde{k}/\widetilde{\varepsilon}$, written as

$$\bar{\rho}\widetilde{\chi}_Z \equiv \overline{\rho D\left(\nabla Z'' \cdot \nabla Z''\right)} \simeq \bar{\rho}\,C_Z\,\frac{\widetilde{Z''^2}}{t_f} \tag{6}$$

and

$$\bar{\rho}\widetilde{\chi}_{Zc} \equiv \overline{\rho D\left(\nabla Z'' \cdot \nabla c''\right)} \simeq \bar{\rho}\,C_{Zc}\,\frac{\widetilde{Z''c''}}{t_f}, \tag{7}$$

where the model coefficients $C_Z = C_{Zc} = 1.0$ are used for this study [1, 21]. For the scalar dissipation rate of progress variable, the algebraic model proposed in [22, 23] is used and

this model is

$$\bar{\rho}\widetilde{\chi}_c \equiv \overline{\rho D (\nabla c'' \cdot \nabla c'')} \simeq \frac{\bar{\rho}}{\beta'}\left([2K_c^* - \tau C_4]\frac{S_L^0}{\delta_L^0} + C_3\frac{\widetilde{\varepsilon}}{\widetilde{k}}\right)\widetilde{c''^2}, \tag{8}$$

where β', C_3 and C_4 are model parameters, which are kept to be the same as in a number of previous studies [5, 6, 22–27]. The other parameters in Eq. (8), K_c^*, τ, S_L^0 and δ_L^0, vary within the flammable mixture range depending on the local equivalence ratio, and these values are obtained from unstrained planar laminar flame calculation as in [5] and [6].

In this present study, the mixture fraction is defined using Bilger's definition [28], in which $Z = 1$ denotes the fuel stream and $Z = 0$ implies the oxidiser stream. For the progress variable, the sum of CO and CO_2 mass fractions, $\psi = Y_{CO} + Y_{CO_2}$, is used as in an earlier study [6] to obtain an unique mapping for the flamelet table. The normalised form of progress variable, $c = \psi / \psi^{Eq}(Z)$, is used so that c is bounded between 0 and 1, and $\psi^{Eq}(Z)$ is the equilibrium value of ψ for the local mixture fraction. This definition allows one to identify individual contributions from premixed and non-premixed combustion modes as detailed in [6].

For turbulence modelling, the simple but yet adequate two-equation $\widetilde{k}$-$\widetilde{\varepsilon}$ model is used with modified model constants to be detailed in section 4. The reaction source terms in Eqs. (3)−(5), $\overline{\dot{\omega}_c^*}$, $\overline{c''\dot{\omega}_c^*''}$ and $\overline{Z''\dot{\omega}_c^*''}$, require modelling and the asterisk * signifies the partially premixed reaction rate detailed in Eq. (9) below. These models are described next.

2.2   *Reaction Rate Modelling*

The mean reaction rate, $\overline{\dot{\omega}_c^*}$, in Eq. (3) is written as [5, 6]

$$\overline{\dot{\omega}_c^*} = \overline{\dot{\omega}}_c + \underbrace{\overline{\rho N_{ZZ}\frac{c}{\psi^{Eq}}\frac{d^2\psi^{Eq}}{dZ^2}}}_{\overline{\omega}_{np}} + \underbrace{\overline{2\rho N_{Zc}\frac{1}{\psi^{Eq}}\frac{d\psi^{Eq}}{dZ}}}_{\overline{\omega}_{cdr}}, \tag{9}$$

where $N_{ZZ} \equiv D_Z(\nabla Z \cdot \nabla Z)$ and $N_{Zc} \equiv D_{Zc}(\nabla Z \cdot \nabla c)$ are the instantaneous mixture fraction dissipation rate and cross dissipation rate. The terms on the RHS, $\overline{\omega}_c$ and $\overline{\omega}_{np}$, signify the contributions of premixed and non-premixed mode combustion respectively. $\overline{\omega}_{cdr}$ denotes contribution arising from the cross dissipation, which is neglected because it is an order of magnitude smaller than the other two contributions [21].

The premixed mode contribution is modelled as [5, 6]

$$\overline{\omega}_c = \bar{\rho} \int_0^1 \int_0^1 \left[\frac{\dot{\omega}_c(\xi, \zeta)}{\rho(\xi, \zeta)}\right] \widetilde{P}(\xi, \zeta) \ d\xi \ d\zeta, \tag{10}$$

where ξ and ζ are the sample space variables for Z and c respectively, and the mean density, $\bar{\rho}$, is obtained using the ideal gas equation of state. The flamelet reaction rate and mixture density, $\dot{\omega}_c(\xi, \zeta)$ and $\rho(\xi, \zeta)$, are obtained from laminar flame calculation. The Favre joint PDF is $\widetilde{P}(\xi, \zeta) = P(\widetilde{Z}, \widetilde{Z''^2}, \widetilde{c}, \widetilde{c''^2}, \widetilde{Z''c''})$. Here the statistical independence between ξ and ζ is not assumed and the *Z-c* correlation is calculated using the *copula* method [5, 23].

A *copula* describes the dependence between the marginal distribution of variables in a multivariate probability distribution [29] . The individual PDF shapes of both the mixture fraction and progress variable can be well represented by the β-distribution [5, 21] and the

correlated joint PDF is constructed using the *copula* involving the two marginal β-PDFs for a given value of $\widetilde{Z''c''}$. Detailed procedure of this approach is described in [5, 23]. Thus, the correlated joint PDF depends on the local statistics of the mixture fraction ($\widetilde{Z}$, $\widetilde{Z''^2}$), progress variable ($\widetilde{c}$, $\widetilde{c''^2}$) and their covariance ($\widetilde{Z''c''}$). In the URANS simulations, these variables are computed through their respective unsteady transport equations accounting for their transient evolution, which is influenced by convective, reactive and diffusive processes.

The second term in Eq. (9), $\overline{\dot{\omega}}_{\text{np}}$, signifying the non-premixed mode combustion contribution is modelled using an algebraic model written as [5, 6]

$$\overline{\dot{\omega}}_{\text{np}} \simeq \overline{\rho} \; \widetilde{c} \; \widetilde{\chi}_Z \int_0^1 \frac{1}{\psi^{\text{Eq}}(\xi)} \frac{d^2\psi^{\text{Eq}}(\xi)}{d\xi^2} \; \widetilde{P}_\beta(\xi) \; d\xi. \tag{11}$$

where $\widetilde{P}_\beta(\xi)$ is the marginal PDF of mixture fraction obtained using Beta function.

For the two source terms in Eq. (4) and (5), $\overline{c''\dot{\omega}_c^{*''}}$ and $\overline{Z''\dot{\omega}_c^{*''}}$, the approximations used in [5, 6] are followed here and these terms are modelled as

$$\overline{c''\dot{\omega}_c^{*''}} \approx \overline{c''\dot{\omega}_c''} \simeq \overline{\rho} \int_0^1 \int_0^1 \left(\zeta - \widetilde{\zeta} \right) \frac{\omega_c(\xi, \zeta)}{\rho(\xi, \zeta)} \; \widetilde{P}(\xi, \zeta) \; d\xi \; d\zeta \tag{12}$$

and

$$\overline{Z''\dot{\omega}_c^{*''}} \approx \overline{Z''\dot{\omega}_c''} \simeq \overline{\rho} \int_0^1 \int_0^1 \left(\xi - \widetilde{\xi} \right) \frac{\omega_c(\xi, \zeta)}{\rho(\xi, \zeta)} \; \widetilde{P}(\xi, \zeta) \; d\xi \; d\zeta. \tag{13}$$

Other Favre averaged themochemical quantities, such as species mass fractions and mixture specific heat capacity are calculated as

$$\widetilde{\phi} = \int_0^1 \int_0^1 \mathcal{F}_\phi(\xi, \zeta) \widetilde{P}(\xi, \zeta) \; d\xi \; d\zeta, \tag{14}$$

where $\mathcal{F}_\phi(\xi, \zeta)$ is the flamelet value for the quantity ϕ. Using the mixture averaged specific heat capacity, $c_{p,mix}$, and the enthalpy of formation, $\Delta h_{f,mix}^0$, the Favre mean temperature, $\widetilde{T}$, is calculated as

$$\widetilde{T} = (\widetilde{h} - \Delta h_{f,mix}^0)/c_{p,mix} + T_0, \tag{15}$$

where $T_0 = 298.15$ K is a reference temperature and the total enthalpy $\widetilde{h}$ is computed using its transport equation as detailed in [5, 6].

These combustion related source terms and themochemical quantities are pre-calculated and tabulated in a flamelet look-up table for turbulent flame simulations of the experimental test case described next.

3. Experimental configuration

Ahmed and Mastorakos [20] conducted an extensive experimental study on lifted methane jet flames for a range of jet velocities and air dilution levels. These lifted flames were stabilised in the downstream of a pure or air-diluted methane jet surrounded by a co-axial laminar airflow. The jet nozzle diameter is 5 mm and the airflow has a diameter of 200 mm with a fixed velocity of 0.1 m/s. The final lift-off heights of these flames have been

computed using 2D RANS simulations [6] and a good agreement with the experiments was observed. The transient evolution of flame position from its initial spark location to final stabilisation is of specific interest for this study. This lifted flame was established in a jet of methane diluted with 30% air by volume. Two bulk mean jet velocities, $U_j = 12.5$ and 25.5 m/s, were recorded with corresponding Reynolds numbers of 3759 and 7669.

In the experiments [20], the open flame was ignited at two downstream locations of 30 and $40d_j$ on the jet centreline. Both high-speed movies and OH PLIF (planar laser-induced fluorescence) techniques are used to visualise the flame evolution processes including from flame kernel growth, expansion, upstream propagation to its final stabilisation at lift-off height. During these processes, the temporal variation of the flame most leading point axial position was examined by line-of-sight images at each elapsed time after ignition. This transient evolution was repeated in 10 experiments for each jet velocity condition and the axial position of the leading point was then ensemble-averaged using these 10 samples. A 9% maximum variation of this axial position was measured for a given elapsed time. It is worth noting here that the line-of-sight image captured by the high-speed movies is the flame evolution in 3D. Thus, the averaged measurements over 10 samples cannot be seen as the average in the azimuthal direction as for the 2D simulations. Therefore, a 3D numerical study is performed to address the objective of this study and the computational setup is described in the next section.

4.   Computational setup

Figure 1 shows a schematic of the numerical setup for the test case. The cylindrical computational domain is $200d_j \times 100d_j \times 2\pi$ in the axial, z, radial, r, and azimuthal, θ, directions. An unstructured grid is used to discretise the computational domain and the mesh in the near field of the jet exit and flame propagation region are refined to resolve the large spatial gradients. The smallest grid cell size of 1.2 mm ($0.24d_j$) is chosen for good computational accuracy and cost based on the study in [6]. As the propagation region ($0-15d_j$ in r and $0-40d_j$ in z directions) is considerably large, the 3D numerical grid consists of 3.2 million tetrahedral cells.

The boundary conditions used in the earlier 2D study [6] are followed for this study also as marked in Figure 1. The mean axial velocity at the jet inlet is specified using the 1/7th power law and the turbulent velocity fluctuation is estimated using a Reynolds correlation [30]. A laminar flow condition is used for the air co-flow with a small velocity of 0.1 m/s as in the experiments [20]. The same condition with the velocity of 0.01 m/s is used for the air entrainment. For the side surface and outlet boundaries, far field boundary condition is used to simulate the open flames. The CFD package ANSYS FLUENT 13.0 is used for the simulations in this study and implementation of the modelling framework is detailed in [5] and [6].

Following the experiments, the numerical ignition is initiated on the jet axis at the location of $40d_j$ downstream of the jet exit for both jet velocities of 12.5 and 25.5 m/s. This location is chosen because it is further away from the jet nozzle, allowing us to study a more complete flame propagation process with varying local mixing conditions. The flame kernel is initialised by setting $\overline{c} = 1$ in a spherical sub-domain with a diameter of 2 mm. The equivalent energy contained in this kernel is about 100 mJ as provided by the electrical spark in the experiments [20]. It was found in [6] that the relative size of the kernel did not affect the final lift-off height and has only marginal influence on the transient flame leading edge evolution. A sensitivity test showed that there is minor influence only in the initial downstream convection stage and the overall flame leading edge evolution remains the same. Refer to [6] for further detail. Note that all the URANS simulations in this study are initialised using this approach on a fully converged cold flow and scalar

mixing solution.

5.   Results and discussion

5.1   *Cold flow results*

A cold air jet with a bulk velocity of 21 m/s (Re = 6800) is simulated first to test and validate the turbulence model and numerical setup. To accurately predict the turbulence for a round jet, the modified constants, $C_\mu = 0.065$, $C_{\varepsilon 1} = 1.44$ and $C_{\varepsilon 2} = 1.85$, used in previous studies [6, 31] are adopted for this work. Figure 2 shows a comparison of the radial variation of mean axial velocity and its r.m.s. (root mean square) values obtained from experiments [20], earlier 2D [6] and the present 3D simulations. The typical results for few axial locations are presented. Note that the radial profiles from 3D simulations are averaged values in the azimuthal, θ, direction. An excellent agreement with the experimental data is seen in this figure for both the mean and r.m.s. of axial velocity. The agreement between 2D and 3D results is also observed in Figure 2 with the 3D simulation showing slightly closer agreement with the experiment especially for the velocity r.m.s values and the difference becomes negligible as one moves downstream. Figure 3 shows the axial velocity variation along the jet centre line. Both 2D and 3D simulations yield good agreement with the empirical relationship established in [32]. These comparisons support the modified parameters used for the turbulence model and validates the boundary conditions used for 3D simulations.

Following the previous studies [6, 18], the computed mean mixture fraction field is compared to an empirical correlation [33] for open jets as shown in Figure 4 and this correlation is written as [33]

$$\widetilde{Z}(\hat{z}, \hat{r}) = 4.76 \, \frac{\sqrt{R_\rho}}{\hat{z}} \exp\left(\frac{-59 \, \hat{r}^{\,2}}{\hat{z}^{\,2}} \right), \tag{16}$$

where R_ρ denotes density ratio of the jet fluid to air, $\hat{z} = (z/d_j - 3.6)$ and $\hat{r} = r/d_j$ are normalised axial and radial coordinates. Figure 4 shows a typical comparison of $\widetilde{Z}$ contours obtained from the correlation and computations for the jet velocity of $U_j = 25.5$ m/s. The equivalence ratio, ϕ, is calculated using $\phi = \widetilde{Z}(1 - \widetilde{Z}_{st})/(\widetilde{Z}_{st}(1 - \widetilde{Z}))$ and $\widetilde{Z}_{st}$ is the stoichiometric mixture fraction. The three iso-lines shown represent the stoichiometry, lean and rich flammability limits respectively for methane-air mixture at 300K. The agreement shown in Figure 4 is better for the 3D simulations compared to the 2D case. These results also suggest that the 2D and 3D reacting flow simulations are initiated from an almost identical cold mixing scenario allowing one to directly investigate the effect of physical dimension on transient evolution of lifted flames.

5.2   *Temporal variation of flame leading edge*

The temporal variation of flame leading edge was measured in [20] using high speed movie techniques and 10 movies covering this transient evolution process from ignition to stabilisation were recorded for each of the two jet velocities of 12.5 and 25.5 m/s. The flame leading point was identified using line-of-sight imaging techniques and the 10 recorded movies were averaged frame by frame to obtain the transient evolution of the leading point of the flame brush. The experimental results for these two velocity cases ignited at $40d_j$ location are shown in Figure 5 along with the computed results obtained from 2D [6] and 3D URANS simulations. The error bar corresponds to the maximum variation of 9% observed in the experiments using limited samples of 10 frames for a

Taylor & Francis and I.T. Consultant

given instant. The most leading point in the 3D simulations is identified using the axial coordinate of the most upstream point of the $\widetilde{T} = 1200$ K iso-surface which corresponds to 5% of the maximum OH concentration as used in [6, 34].

In Figure 5, the y-axis is the axial coordinate normalised using the fuel jet diameter, and the x-axes are non-dimensional time axes corresponding to the elapsed time after ignition. The time axes, t^* and t^+, are scaled respectively using a jet flow time-scale defined as (d_j/U_j) and a laminar flame time-scale $\tau_L \equiv (\delta_L^0/S_L^0) \simeq 1.2 \times 10^{-3}$ s for stoichiometric methane-air mixture. As shown in this figure, the downstream convection movement of the initial flame kernel and the flame final lift-off height are captured well by the 3D computations, similar to that observed in the earlier 2D study. This suggests that the final lift-off height, as a steady-state flame characteristic, is not influenced by the physical dimensions. However, a substantial improvement is seen for the transient flame propagation process for both $U_j = 25.5$ and 12.5 m/s cases shown respectively in Figures 5a and 5b. The flame brush propagation speed given by the slopes of these curves seems to agree better with the experimental data for the 3D cases compared to 2D results as one shall see while discussing Figure 6. As has been shown in Figure 13 of [6], after ignition at far downstream locations the flame first propagates in a fully flammable region before it encounters non-flammable mixtures from both rich and lean sides. This instant can be seen at $t^+ \sim 450$ in Figure 5a and $t^+ \sim 250$ in Figure 5 (b), where the experimental data points start to show horizontal bending suggesting a reduction in the propagation speed. This sub-process is well predicted by 3D simulations showing good agreement for the "bending point" for both jet velocities. In contrast, this appears much earlier in 2D simulations, at $t^+ \sim 200$ and $t^+ \sim 100$ for $U_j = 25.5$ and 12.5 m/s respectively. This is due to a quicker propagation of the flame brush in 2D simulations as seen in Figures 5a and 5b. This is more evident during the initial propagation in which the mixture surrounding the flame leading edge is within the flammability limits. This process is often referred to as stratified flame propagation [1, 9] since the premixed combustion with varying equivalence ratios is found to be dominant. The influence of physical dimension observed here suggests that the third physical dimension plays an important role in flames propagating in partially premixed mixtures. To shed more light on this, the effect of the third physical dimension on flame brush propagation speed is studied next.

5.3   *Flame brush propagation characteristics*

Flame displacement speed is known as the speed at which the flame front moves normal to its surface, relative to the local flow velocity [1]. Its behaviours in response to various parameters, such as curvature and stretching effects, can be studied both morphologically and statistically using DNS approaches as mentioned earlier in this paper. However, it is rather difficult to accurately identify the flame front in experiments using the existing diagnostic techniques. For numerical simulations involving statistical models, namely RANS and LES, the flame front is theoretically unavailable. Because the flame front is not fully resolved but averaged as a "flame brush" (RANS) or filtered as a "filtered flame" (LES). Therefore, the flame brush displacement speed, $\overline{S}_d$, computed using unsteady RANS is investigated here.

5.3.1   *Net flame propagation speed*

In the experimental study of Ahmed and Mastokaros [20], an ensemble averaged net flame propagation speed, $\overline{S}_{net}$, with respect to the laboratory coordinates was calculated using differentiation of fifth-order polynomial curve fit based on the measured points as shown in Figure 5. The same curve fitting method is used for the temporal variations obtained from the 2D and 3D simulations and these results are compared in Figure 6 for both $U_j =$

25.5 and 12.5 m/s cases. Note that this propagation speed accounts for the axial component of the flame brush displacement speed subtracted by the local flow axial velocity written as

$$\overline{S}_{\text{net}} = -(\overline{S}_{\text{d}}\mathbf{n} + \boldsymbol{U}) \cdot \mathbf{k}, \tag{17}$$

where $\mathbf{n} = -\nabla\widetilde{c}/|\nabla\widetilde{c}|$ is the unit normal vector of the flame brush surface pointing towards the unburnt gas and $\mathbf{k}$ denotes the unit vector in z-direction pointing towards the downstream of the jet flow. In this figure, the experimental results show that $\overline{S}_{\text{net}}$ for the low jet velocity (12.5 m/s) case is approximately 2 times of that for high velocity (25.5 m/s) during the entire flame evolution process. This is consistent with the scaling analysis in [6] showing that the time taken to reach the final lift-off height is proportional to the jet velocity using the normalised time-scale, $t^+ = t/\tau_{\text{L}}$. τ_{L} is the stoichiometric methane-air flame time-scale and t is the elapsed wall-clock time after ignition. Therefore, it provides further support to the argument that the premixed flame propagation plays a vital role in the establishment of lifted flame from an initial flame kernel.

Figure 6 also shows that the 3D simulation results for $\overline{S}_{\text{net}}$ agree quite well with the experimental data, whereas significant discrepancies are observed for 2D simulations especially in the early stages (large z/d_{j} values). This is particularly apparent for the axial positions ranging from the ignition point, $z = 40d_{\text{j}}$ to about $20d_{\text{j}}$ for $U_{\text{j}} = 25.5$ m/s, and to about $10d_{\text{j}}$ for $U_{\text{j}} = 12.5$ m/s. These axial positions correspond to the "bending points" noted while discussing Figure 5. After passing these positions, these three curves tend to converge towards the final lift-off height.

After the ignition, the flame brush tends to propagate towards the upstream at a nearly constant $\overline{S}_{\text{net}}$ initially and then slows down after encountering the region where the partial premixing with non-flammable mixtures starts to affect the leading edge propagation. This trend is captured reasonably well in 3D simulations as seen in Figure 6, however, the net propagation speed computed in the 2D simulations shows a constant descending trend from the ignition to final stabilisation point.

These differences must stem from the influences of physical dimension on the displacement speed, $\overline{S}_{\text{d}}$, since $\widetilde{U}$ is observed to be reasonably similar in 2D and 3D cases (see Figure 2). These effects are discussed next.

5.3.2   *Displacement speed components*

The transport equation of $\widetilde{c}$ in Eq. (3) can be written in propagative form as

$$\overline{\rho}\frac{\partial\widetilde{c}}{\partial t} + \overline{\rho}(\widetilde{U} + \overline{S}_{\text{d}}\mathbf{n}) \cdot \nabla\widetilde{c} = 0, \tag{18}$$

where the flame brush displacement speed, $\overline{S}_{\text{d}}$, is

$$\overline{S}_{\text{d}} = \frac{\nabla \cdot (\mu_{\text{eff}}\nabla\widetilde{c}) + \overline{\dot{\omega}_c^*}}{\overline{\rho}|\nabla\widetilde{c}|}. \tag{19}$$

The effective dynamic viscosity is given as $\mu_{\text{eff}} = \mu + (\mu_{\text{t}}/\text{Sc}_{\text{t}})$, where μ and μ_{t} are the laminar and turbulent viscosity respectively and $\text{Sc}_{\text{t}} \approx 0.7$ is the turbulent Schmidt number.

The displacement speed is decomposed into three components as [1, 35]

$$\overline{S}_{\text{d}} = \overline{S}_{\text{n}} + \overline{S}_{\text{t}} + \overline{S}_{\text{r}}. \tag{20}$$

$\overline{S}_n$ is the normal diffusion component written as

$$\overline{S}_n = \frac{\mathbf{n} \cdot \nabla (\mu_{\text{eff}}\, \mathbf{n} \cdot \nabla \widetilde{c})}{\overline{\rho}\, |\nabla \widetilde{c}|} \,, \tag{21}$$

In the jet flame configuration of this paper, $\mathbf{n}$ at the leading edge of the flame brush points towards the upstream in the $-z$ direction.

The tangential diffusion component is given by

$$\overline{S}_t = -\frac{\mu_{\text{eff}}\, (\nabla \cdot \mathbf{n})}{\overline{\rho}} \,, \tag{22}$$

where $(\nabla \cdot \mathbf{n})$ is the mean curvature of the flame surface which may also be written as the sum of the two principle curvatures, $(\kappa_1 + \kappa_2)$, as in previous studies[1, 35].

Finally, $\overline{S}_r$ is the the reaction component written as

$$\overline{S}_r = \frac{\overline{\dot{\omega}_c^*}}{\overline{\rho}\, |\nabla \widetilde{c}|} \,. \tag{23}$$

The numerical values of these speeds depend on $\widetilde{c}$ iso-surface and their values at the leading edge marked using $\widetilde{c} = 0.05$ are of interest here. As the displacement speed is defined as the relative flame propagation speed normal to the local flame surface, the propagation direction of $\overline{S}_d$ and its components vary across the flame brush during the lifted flame evolution. Figure 7 presents the colour map of the progress variable field and mixture fraction iso-contours obtained from the 2D and 3D computations at the same axial position of about $30d_j$ for the flame brush leading edge. This corresponds to a time instant of $t^+ = 70$ for the 2D and $t^+ = 150$ for the 3D flames as can ben seen in Figure 5. The leading edge is marked using the iso-surface of $\widetilde{c} = 0.05$ shown as a dashed line in Figure 7. This value of $\widetilde{c} = 0.05$ has been used in earlier turbulent flame speed studies [36, 37] and is followed here. The arrows correspond to the local flame normal direction, $\mathbf{n}$, on the leading edge. Note that both cases are initialised at an axial distance of $40d_j$ with the same jet velocity of $U_j = 25.5$ m/s for comparison. From this figure, one can see that the flame brush has similar shape between the 2D and 3D computations at the same axial position even with a different evolution in time from the ignition position. It is also shown that the flame normal direction, $\mathbf{n}$, varies along the leading edge suggesting different propagation direction locally. Note that $\mathbf{n}$ points towards exactly the upstream, $(-z)$ direction, at the leading point which is located in the lean mixture with $\widetilde{Z} \simeq 0.08$ experiencing relatively low flow velocity. The leading edge with the stoichiometric mixture propagates towards the jet centreline as indicated in Figure 7 and it experiences relatively high flow velocity. Thus, the leading point always has the highest net propagation speed and remains as the most upstream point on the leading edge. As a result, the net propagation speed defined in Eq. (17) at the leading point is determined by the leading point propagation characteristics such as the local flow velocity, displacement speed and their directions. This is further discussed later while examining $\overline{S}_d$ and its components at the leading point.

The computed contours of $\overline{S}_r$, $\overline{S}_n$ and $\overline{S}_t$ are shown in Figure 8 for both the 2D and 3D cases at the same axial position as in Figure 7. The mixture fraction contours (solid lines) correspond to the stoichiometry, $\widetilde{Z}_{st}$, and flammability limits for lean, $\widetilde{Z}_l$, and rich, $\widetilde{Z}_r$, methane-air mixtures. A progress variable iso-surface for $\widetilde{c} = 0.05$ (dashed line) representing the flame leading edge is also highlighted in this figure.

The reaction contribution to the propagation is concentrated at a downstream location of about $32\, d_j$ as seen in Figures 8a and 8d, where the maximum value is about 6m/s $\sim$ $15S_L^0$ in both the 2D and 3D cases. The value of $\overline{S}_r$ at the leading edge is much smaller,

which is about $2.5S_L^0$. Therefore in this process, the diffusion (both laminar and turbulent) plays a rather important role by bringing the highly reactive radicals and heat from the downstream to the leading edge. Furthermore, no substantial influence of the physical dimension is observed at the leading edge between Figures 8a and 8d as one would expect, however, the region with high $\overline{S}_r$ values in the 2D case seems to be larger than that in the 3D case. Since $\tilde{\omega}_c^*$ does not depend on the physical dimension, the difference in the scalar gradient magnitude, $|\nabla \tilde{c}|$, between the 2D and 3D is the cause for the differences in $\overline{S}_r$ (see Eq. (23)).

Figures 8b and 8e show the spatial variation of the normal diffusion component in the 2D and 3D simulations respectively. In both figures, $\overline{S}_n$ varies from positive to negative values along the stoichiometric iso-line respectively from the upstream to downstream positions through the flame brush. The change of sign occurs in the middle of the flame brush at almost $\tilde{c} = 0.5$. Note that positive value implies a positive contribution to the propagation towards the unburnt side and *vice versa*. The positive maximum values of $\overline{S}_n$ are located around $\tilde{c} = 0.05$ iso-contour, suggesting that this is an important contribution to the flame leading edge propagation. These maximum values are around 0.4-0.6 m/s, which is close to the laminar flame burning velocity.

The tangential diffusion component, $\overline{S}_t$, is plotted in Figures 8c and 8f for the 2D and 3D cases respectively. Similar variation as for $\overline{S}_n$ is seen, but with the maximum values of around 0.2 m/s, much smaller than that of $\overline{S}_n$ and $\overline{S}_r$. The large positive $\overline{S}_t$ values are located further towards the upstream at approximately $\tilde{c} = 0.01$ where the flow field starts to diverge as indicated by the $\tilde{Z}$ contours.

In order to examine the displacement speed at the leading edge more quantitatively, the profiles of $\overline{S}_d$ components are plotted against the mixture fraction, $\tilde{Z}$, along the dot-dashed line shown in Figure 8d at different axial positions. These profiles are presented in Figure 9 for both velocities, U_j =25.5 and 12.5 m/s. The range of $\tilde{Z}$ is shown from the lean limit, $\tilde{Z}_l = 0.05$, to the stoichiometric value, $\tilde{Z}_{st} = 0.098$ and the leading edge is highlighted using a vertical dashed line. The axial velocity profiles are also presented to examine the balance between the displacement speed and the flow velocity shown in Eq. (18). Note that the y-axis is normalised using the laminar flame speed for stoichiometric methane-air mixture, S_L^0. Moving from the top to bottom in Figure 9, the axial position, z/dj, reflects the transient evolution of the leading edge propagation starting from the far downstream position of z/dj=30 towards the upstream and finally stabilises at the lift-off height position.

As expected from the earlier discussion, it is more evident in this figure that the tangential diffusion component, $\overline{S}_t$, is always less than $0.5S_L^0$, relatively small compared to the other two components throughout the flame evolution process for both velocities. Despite the difference between the 2D and 3D results for $\overline{S}_t$, the contribution of this component is too weak to substantially influence the flame propagation speed. The other two dominant components, $\overline{S}_r$ and $\overline{S}_n$, both have peaks located close to the leading point at all plotted positions. The values of both $\overline{S}_r$ and $\overline{S}_n$ at the leading point for the 2D cases are higher compared to that for 3D. For both velocity cases, this difference is substantial in the early stage of the transient evolution (top two rows in Figure 9), whereas it vanishes as the leading edge approaches the final lift-off height region. As the local velocity is similar as shown by the coloured lines, the leading edge propagation speed in the 2D simulation is higher than that of 3D simulation in the early stage as has already been shown in Figure 6. However, as the flame brush propagates upstream, the profiles of $\overline{S}_r$ and $\overline{S}_n$ spread over the mixture fraction space with smaller peak values near the leading edge and finally become more or less flat at the final lift-off height showing a fine balance between the flow velocity and the flame displacement speed for both 2D and 3D computations. The same trend is observed in Figure 9 for both jet velocities. Thus, this change

of influence of physical dimension during the transient evolution process is interpreted as that in the early-stage premixed propagation, since the surrounding mixture are fully flammable, the evolution of spatial gradients of scalars such as $\nabla \widetilde{c}$, plays a vital role in the flame propagation. As this spatial evolution occurs in the 3D physical space, one would expect 3D simulation for accurate prediction. However, these spatial gradients become less important to the leading edge propagation in the later edge flame propagation stage, involving many other physical processes such as strong flame/turbulence interaction, partial premixing with non-flammable mixtures, etc. In this stage, 2D simulation shows a reasonable prediction in the balance of these processes at the final lift-off height.

Another notable point in Figure 9 is that the peak value of $\overline{S}_n$ is nearly constant around S_L^0 throughout the flame evolution process, namely about 0.5 and 0.3 m/s for $U_j = 25.5$ and 12.5 m/s respectively. In contrast, the maximum value of $\overline{S}_r$ decreases quite significantly as the leading edge propagates towards its final stabilisation height. For both velocities, it drops from a value of several times of S_L^0 to around 0.4 m/s, which is very close to S_L^0. This is in line with the argument of Müller *et al.* [9] using a G-equation approach showing that the premixed flame propagation dominates the early stage propagation process and the final stabilisation is controlled by a fine balance between many complex physical processes.

Finally, to investigate the scalar gradients directly Figure 10 shows the profiles of $|\nabla \widetilde{c}| \delta_L^0$ in the $\widetilde{Z}$ space and δ_L^0 is the laminar flame thickness for stoichiometric methane-air mixture. It is seen that the value of $|\nabla \widetilde{c}| \delta_L^0$ at the leading point for the 3D computation is higher than that for the 2D case at most axial positions except those close to the final lift-off height. This is consistent with the previous findings in Figures 8 and 9, where the peak values of $\overline{S}_r = \overline{\dot{\omega}_c^*} / \overline{\rho} |\nabla \widetilde{c}|$ at high axial positions, are smaller for the 3D simulation. It is also seen that for both velocity cases the maximum $|\nabla \widetilde{c}| \delta_L^0$ values vary only marginally throughout the transient evolution process. This suggests that the decrease of peak value $\overline{S}_r$ shown in Figure 9 is caused by the decrease of maximum reaction rate at the leading edge, which may be due to the stronger turbulent fluctuations close to the jet nozzle corresponding to higher value of $|\nabla \widetilde{Z}|$, which agrees with a previous DNS study [17] showing that increase of mixture fraction gradient leads to decrease of S_r. Furthermore, $|\nabla \widetilde{c}| \delta_L^0$ spreads over a wider range of mixture fraction at the leading edge as the flame propagates towards the upstream. In the stratified propagation stage (top two rows), the gradient of $\widetilde{c}$ is mostly contained within the flammability limits suggesting that this scalar gradient is mainly driven by the chemical reactions. However, in the stabilisation stage (bottom two rows) the gradient covers a wider range beyond the flammability limits. This phenomenon indicates that in the stabilisation region, flame/flow interaction becomes much stronger and starts to influence the flame leading edge structure.

6.   Conclusions

Unsteady RANS simulations of spark ignited turbulent methane/air jet flames are performed using a partially premixed combustion model [5, 6]. An earlier study [6] has shown that the transient evolution of the lifted flame from ignition to stabilisation cannot be fully captured by 2D URANS and thus 3D simulations are used in this study. A diluted jet with 70% CH_4 and 30% air by volume, injected into ambient air in the experimental study [20] is tested for two jet bulk velocities, $U_j = 25.5$ and 12.5 m/s. Following the experiment and 2D simulation, the jet is ignited at a far downstream axial position of $z/d_j = 40$ allowing a complete evolution process from initial ignition to final stabilisation. The 3D computational results are then compared to the experimental and previous 2D results. The main findings of the present study are summarised as follows.

- As one would expect, same final lift-off height is obtained from 2D and 3D computations for both jet velocities showing a good agreement with the experiments [20]. This suggests that the influence of the third physical dimension on the flame stabilisation is negligible and hence the axisymmetric assumption is quite reasonable for computation of steady-state final lift-off height.

- Compared to the previous 2D results [6], the 3D computation shows an evident improvement in comparison to the experimental data for the unsteady evolution of the most upstream point of flame leading edge. The computed 3D net propagation speed is found to be much closer to the measured value. This is especially evident in the initial stage after ignition where the premixed flame propagation dominates for mixtures within the flammability limits. The third physical dimension plays an important role in this process by allowing the flame to evolve in the three-dimensional space, which leads to different flame propagation characteristics compared to 2D simulation. This influence of physical dimension is then found to be less significant after entering a region close to the final stabilisation height.

- Flame brush displacement speed, $\overline{S}_d$, at the leading edge is investigated and it is found that for both 2D and 3D cases, the tangential diffusion component of $\overline{S}_d$ is much smaller than the reaction, $\overline{S}_r$, and normal diffusion, $\overline{S}_n$, components throughout the transient flame evolution. The values of $\overline{S}_r$ and $\overline{S}_n$ in the 2D simulations are found to be larger than those of the 3D cases resulting in a higher net propagation speed. This effect of physical dimension is found to be more evident in the initial stratified flame propagation stage.

- The progress variable gradient $\nabla\widetilde{c}$ at the flame leading point is larger in the 3D cases compared to that for the 2D cases. From the initial ignition to the final stabilisation, the maximum value of $|\nabla\widetilde{c}|\delta_L^0$ is found to be approximately the same, which implies that the higher mixture fraction gradient, $\nabla\widetilde{Z}$, resulting in the smaller reaction component of the displacement speed is responsible for the observed decrease of $\overline{S}_r$.

Although the three-dimensional unsteady RANS simulation using a partially premixed combustion model seems to show quite good capabilities of predicting the transient evolution of the flame leading point, the instantaneous features of edge flame propagation and its interaction with the large structures of the oncoming flow are still to be examined. The influence of the third physical dimension is seen but still in an averaged manner in 3D URANS. Therefore, instantaneous behaviours of flame leading edge dynamics in the azimuthal direction remains to be explored and more advanced approaches such as LES is well suited for this.

Acknowledgement

References

[1] N. Peters, *Turbulent Combustion*, Cambridge University Press, 2000.

[2] W.M. Pitts, *Assessment of theories for the behavior and blowout of lifted turbulent jet diffusion flames*, Proc. Combust. Inst. 22 (1988), pp. 809–816.

[3] K.M. Lyons, *Toward an understanding of the stabilization mechanisms of lifted turbulent jet flames: Experiments*, Prog. Energy Combust. Sci. 33 (2007), pp. 211–231.

[4] C.J. Lawn, *Lifted flames on fuel jets in co-flowing air*, Prog. Energy Combust. Sci. 35 (2009), pp. 1–30.

REFERENCES

[5] S. Ruan, N. Swaminathan, and O.R. Darbyshire, *Modelling of turbulent lifted jet flames using flamelets: a priori assessment and a posteriori validation*, Combust. Theory Model. 18 (2014), pp. 295–329.

[6] Z. Chen, S. Ruan, and N. Swaminathan, *Simulation of turbulent lifted methane jet flames: effects of air-dilution and transient flame propagation*, Combust. Flame 162 (2015), pp. 703–716.

[7] D. Bradley, P.H. Gaskell, and A.K.C. Lau, *A mixedness-reactedness flamelet model for turbulent diffusion flames*, Proc. Combust. Inst. 23 (1990), pp. 685–692.

[8] J.-B. Michel, O. Colin, C. Angelberger, and D. Veynante, *Using the tabulated diffusion flamelet model adf-pcm to simulate a lifted methane-air jet flame*, Combust. Flame 156 (2009), pp. 1318–1331.

[9] C.M. Müller, H. Breitbach, and N. Peters, *Partially premixed turbulent flame propagation in jet flames*, Proc. Combust. Inst. 25 (1994), pp. 1099–1106.

[10] C.B. Devaud and K.N.C. Bray, *Assessment of the applicability of conditional moment closure to a lifted turbulent flame: first order model*, Combust. Flame 132 (2003), pp. 102–114.

[11] T. Poinsot and D. Veynante, *Theoretical and Numerical Combustion*, 2nd ed., Edwards, 2005.

[12] N. Swaminathan and K.N.C. Bray (eds.), *Turbulent premixed flames*, Cambridge University Press, 2011.

[13] J.F. Driscoll, *Turbulent premixed combustion: Flamelet structure and its effect on turbulent burning velocities*, Prog. Energy Combust. Sci. 34 (2008), pp. 91–134.

[14] H.G. Im and J.H. Chen, *Effects of flow strain on triple flame propagation*, Combust. Flame 126 (2001), pp. 1384–1392.

[15] C.S. Yoo and H.G. Im, *Transient dynamics of edge flames in a laminar nonpremixed hydrogen–air counterflow*, Proc. Combust. Inst. 30 (2004), pp. 349–356.

[16] C. Pantano, *Direct simulation of non-premixed flame extinction in a methane–air jet with reduced chemistry*, J. Fluid Mech. 514 (2004), pp. 231–270.

[17] N. Chakraborty and E. Mastorakos, *Numerical investigation of edge flame propagation characteristics in turbulent mixing layers*, Phys. Fluids 18 (2006), p. 105103.

[18] G. Lacaze, E. Richardson, and T. Poinsot, *Large eddy simulation of spark ignition in a turbulent methane jet*, Combust. Flame 156 (2009), pp. 1993–2009.

[19] W.P. Jones and V.N. Prasad, *Les-pdf simulation of a spark iginited turbulent methane jet*, Proc. Combust. Inst. 33 (2011), pp. 1355–1363.

[20] S.F. Ahmed and E. Mastorakos, *Spark ignition of lifted turbulent jet flames*, Combust. Flame 146 (2006), pp. 215–231.

[21] S. Ruan, N. Swaminathan, K.N.C. Bray, Y. Mizobuchi, and T. Takeno, *Scalar and its dissipation in the near field of turbulent lifted jet flame*, Combust. Flame 159 (2012), pp. 591–608.

[22] H. Kolla, J.W. Rogerson, N. Chakraborty, and N. Swaminathan, *Scalar dissipation rate modeling and its validation*, Combust. Sci. Technol. 181 (2009), pp. 518–535.

[23] O.R. Darbyshire and N. Swaminathan, *A presumed joint pdf model for turbulent combustion with varying equivalence ratio*, Combust. Sci. Technol. 184 (2012), pp. 2036–2067.

[24] O.R. Darbyshire, N. Swaminathan, and S. Hochgreb, *The effects of small-scale mixing models on the prediction of turbulent premixed and stratified combustion*, Combust. Sci. Technol. 182 (2010), pp. 1141–1170.

[25] I. Ahmed and N. Swaminathan, *Simulation of spherically expanding turbulent premixed flames*, Combust. Sci. Technol. 185 (2013), pp. 1509–1540.

[26] I. Ahmed and N. Swaminathan, *Simulation of turbulent explosion of hydrogen-air mixtures*, J. Hydrogen Energy 39 (2014), pp. 9562–9572.

[27] S. Ruan, N. Swaminathan, M. Isono, T. Saitoh, and K Saitoh, *Simulation of premixed combustion with varying equivalence ratio in gas turbine combustor*, J. Propulsion Power 31 (2015), pp. 861–871.

[28] R.W. Bilger, S.H. Stårner, and R.J. Kee, *On reduced mechanisms for methane-air combustion in nonpremixed flames*, Combust. Flame 80 (1990), pp. 135–149.

[29] R.B. Nelsen, *An introduction to copulas*, Springer, 1999.

[30] D.C. Wilcox, *Turbulence Modeling for CFD*, DCW Industries, Inc., 2006.

[31] W.P. Jones and M. Kakhi, *Pdf modeling of finite-rate chemistry effects in turbulent nonpremixed jet flames*, Combust. Flame 115 (1998), pp. 210–229.

[32] S.R. Tieszen, D.W. Stamps, and T.J. O'Hern, *A heuristic model of turbulent mixing applied to blowout of turbulent jet diffusion flames*, Combust. Flame 106 (1996), pp. 442–466.

[33] C.D. Richards and W.M. Pitts, *Global density effects on the self-preservation behaviour of turbulent free jets*, J. Fluid Mech. 254 (1993), pp. 417–435.

[34] M.S. Mansour, *Stability characteristics of lifted turbulent partially premixed jet flames*, Combust. Flame 133 (2003), pp. 263–274.

[35] N. Peters, P. Terhoeven, J.H. Chen, and T. Echekki, *Statistics of flame displacement speeds from computations of 2-d unsteady methane-air flames*, Proc. Combust. Inst. 27 (1998), pp. 833–839.

[36] T.D. Dunstan, N. Swaminathan, and K.N.C. Bray, *Influence of flame geometry on turbulent premixed flame propagation: a dns investigation*, J. Fluid Mech. 709 (2012), pp. 191–222.

[37] T.D. Dunstan, N. Swaminathan, K.N.C. Bray, and R.S. Cant, *Geometrical properties and turbulent flame speed measurements in stationary premixed v-flames using direct numerical simulation*, Flow Turbulence Combust. 87 (2011), pp. 237–259.
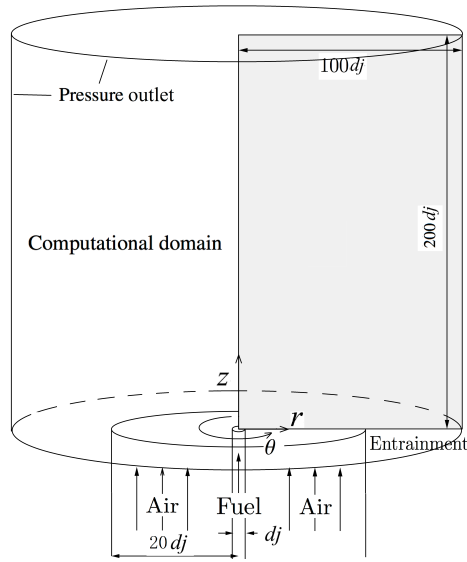
Figure 1. Schematic of numerical setup for the jet burner of the experiments in [20].
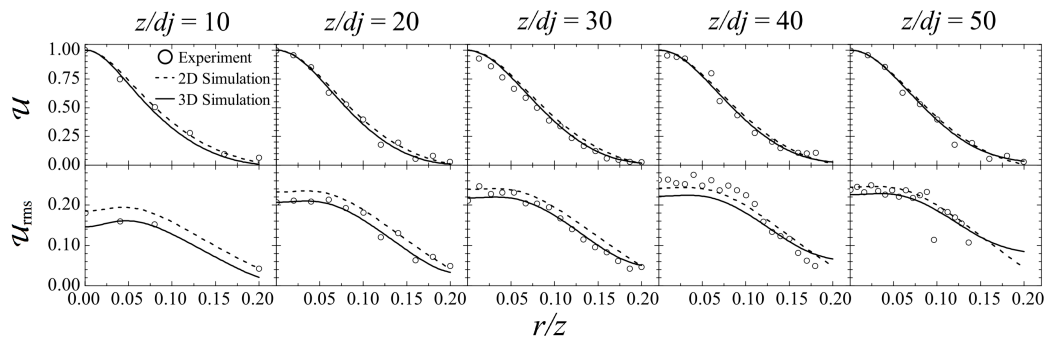

Figure 2.   Comparison of radial variation of axial mean velocity and r.m.s values obtained from the experiments [20], 2D [6] and 3D computations. The radius is normalised using z. The mean velocity is scaled as $\mathcal{U} = (\widetilde{U} - U_c)/(\widetilde{U}_{cl} - U_c)$, where $U_c = 0.1$ m/s is the co-flow velocity and $\widetilde{U}_{cl}$ is the centreline value at the respective z location. The r.m.s. value is scaled as $\mathcal{U}_{rms} = u_{rms}/(\widetilde{U}_{cl} - U_c)$ and $u_{rms} = (2\widetilde{k}/3)^{1/2}$.
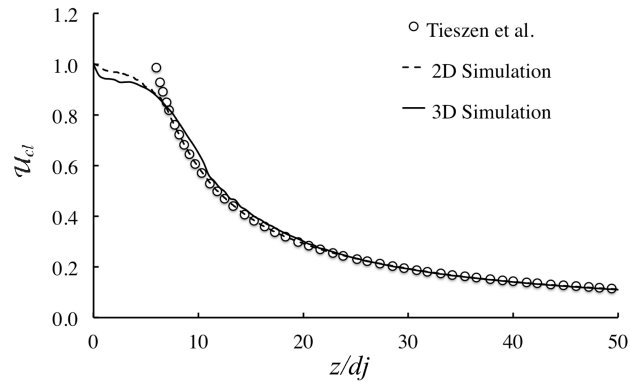
Figure 3.   Axial variation of scaled jet centreline velocity, $\mathcal{U}_{cl} = (\overline{U}_{cl} - U_c)/(U_j - U_c)$. The computed result is compared with the previous 2D study [6] and an empirical correlation [32].
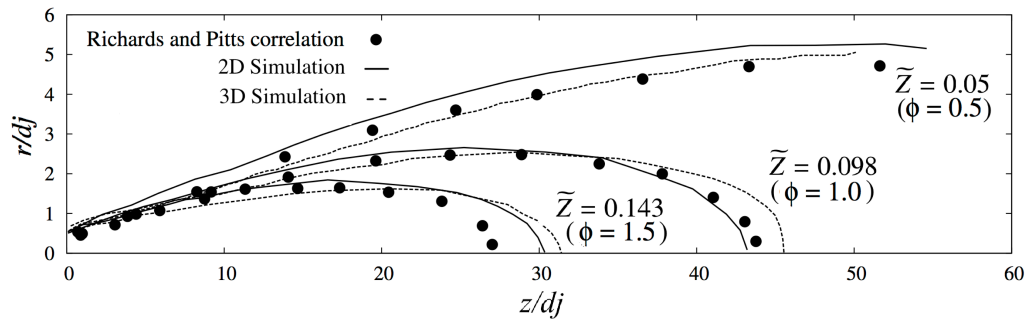
Figure 4.   Comparison of equivalence ratio, ϕ, contours computed from 2D [6] and 3D RANS simulations and calculated using a correlation [33] for U_j=25.5 m/s.
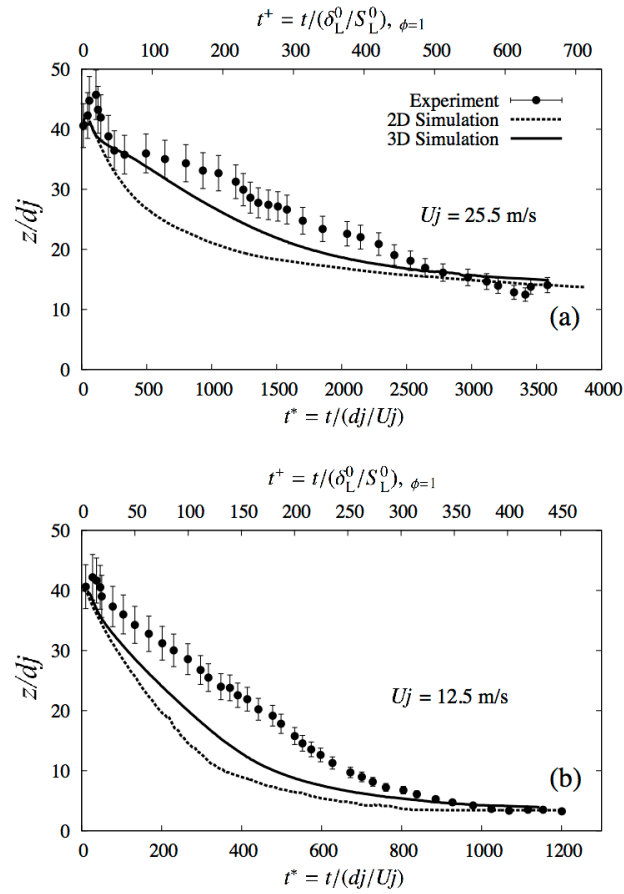
Figure 5. Temporal variation of axial location of flame leading edge, marked using the most upstream point of $\widetilde{T} = 1200$ K contour. Ignition was conducted at the instant $t = 0$. The error bar corresponds to 9% maximum error reported in [20].
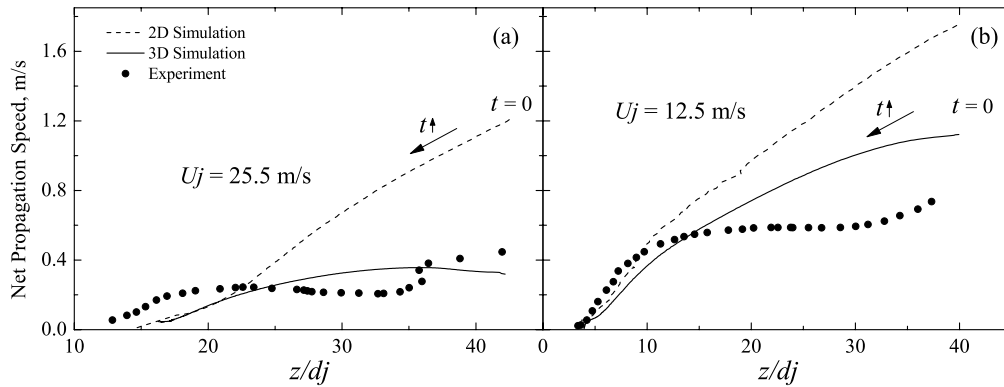
Figure 6. Comparison of net flame propagation speed vs. axial position, calculated from the results shown in Figure 5 using best curve fits.
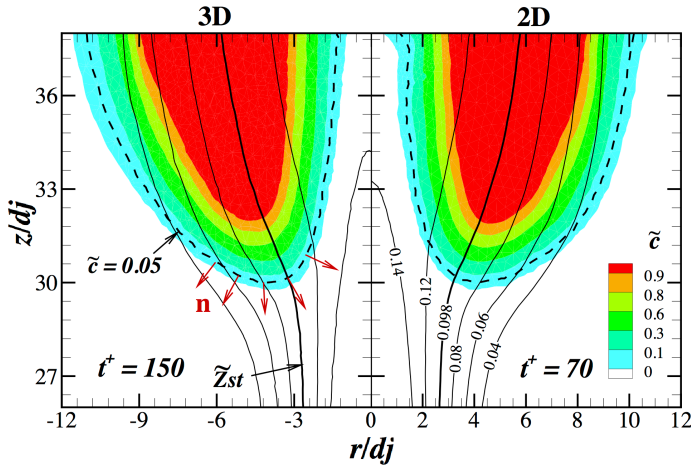
Figure 7.   Computed 3D (left) and 2D (right) progress variable field at axial position, z/d_j=30, for U_j=25.5 m/s. The flame leading edge is marked using the iso-surface of $\widetilde{c} = 0.05$ shown as a dashed line. The solid lines are mixture fraction contours with stoichiometry, $\widetilde{Z}_{st} = 0.098$, being the thick line. The arrows correspond to local flame normal direction on the leading edge. Note the 3D contour is obtained from a slice on the middle plane of the domain.
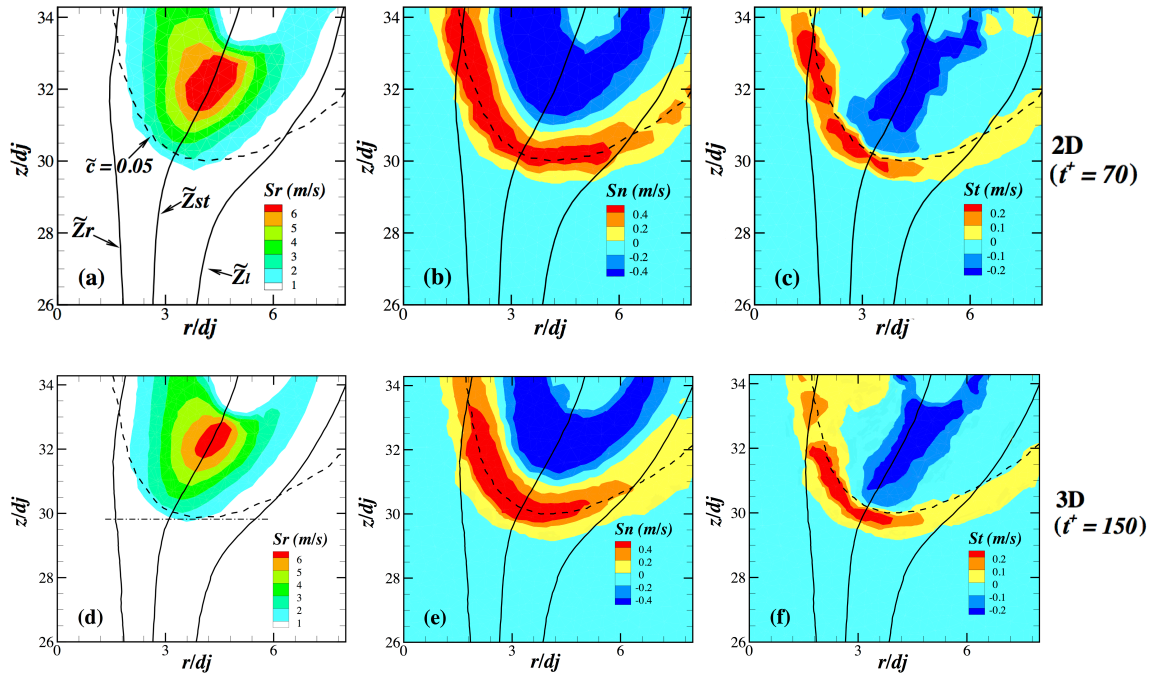

Figure 8.   Spatial variation of displacement speed components, $\overline{S}_r$ (reaction), $\overline{S}_n$ (normal diffusion) and $\overline{S}_t$ (tangential diffusion) obtained from 2D (top row) and 3D (bottom row) simulations. The 3D contour is obtained from a slice on the middle plane of the domain. Mean mixture fraction iso-contours are shown as black solid lines for stoichiometry ($\widetilde{Z}_{st}$), and flammability limits for lean ($\widetilde{Z}_l$) and rich ($\widetilde{Z}_r$) mixtures. The dashed line is the progress variable iso-surface of $\widetilde{c} = 0.05$. The jet exit velocity is $U_j = 25.5$ m/s.
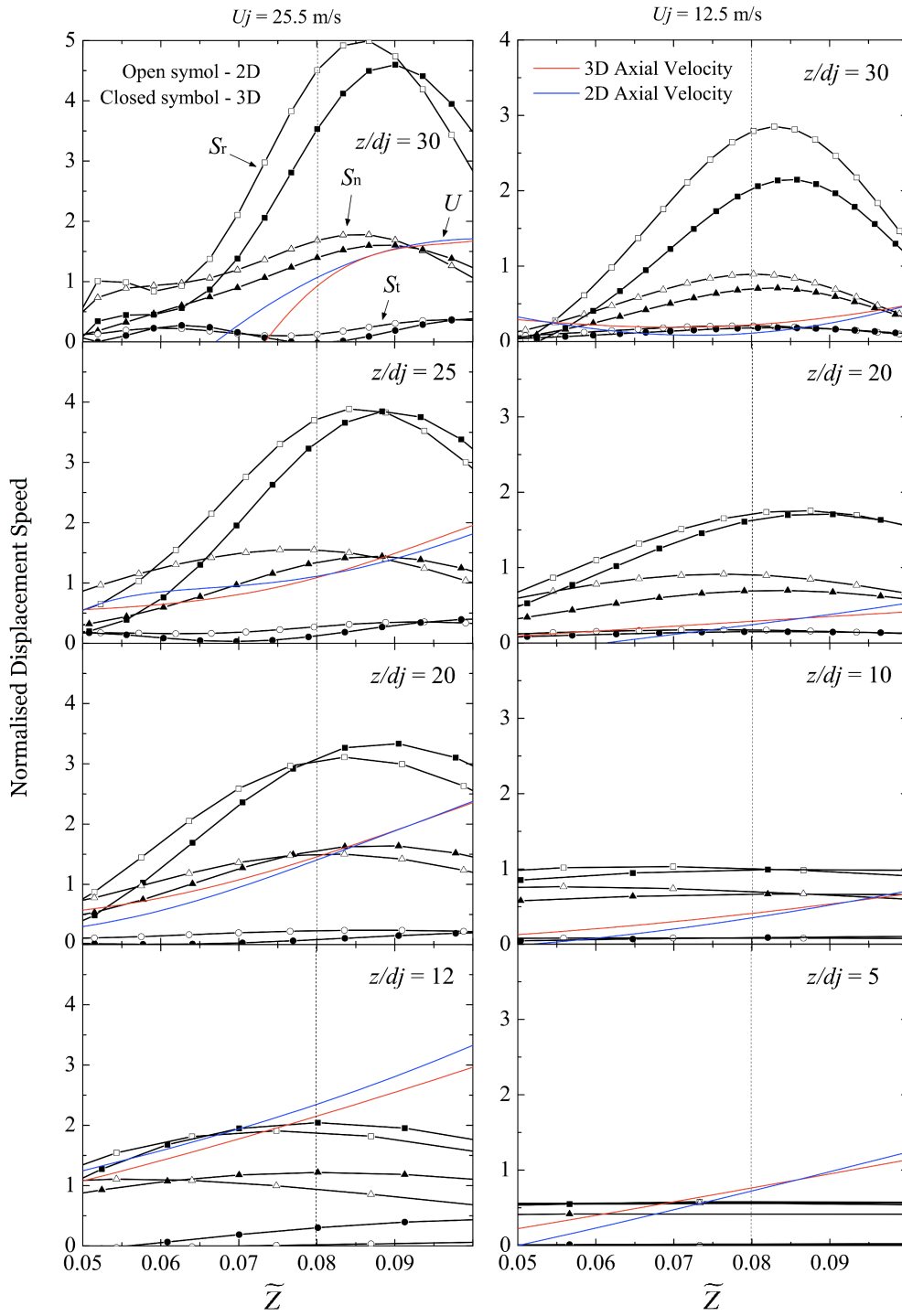
Figure 9.   Comparison of computed 2D (open symbol) and 3D (closed symbol) displacement speed components in the mixture fraction space at different axial positions. The mean axial velocity is shown using blue (2D) and red (3D) solid lines. The y-axis is normalised using the laminar flame speed for stoichiometric methane-air mixture, S_L^0. Two jet velocities, $U_j = 25.5$ m/s (left column) and 12.5 m/s (right column) are considered. The vertical dashed line corresponds to the flame most leading point marked in Figure 8d.
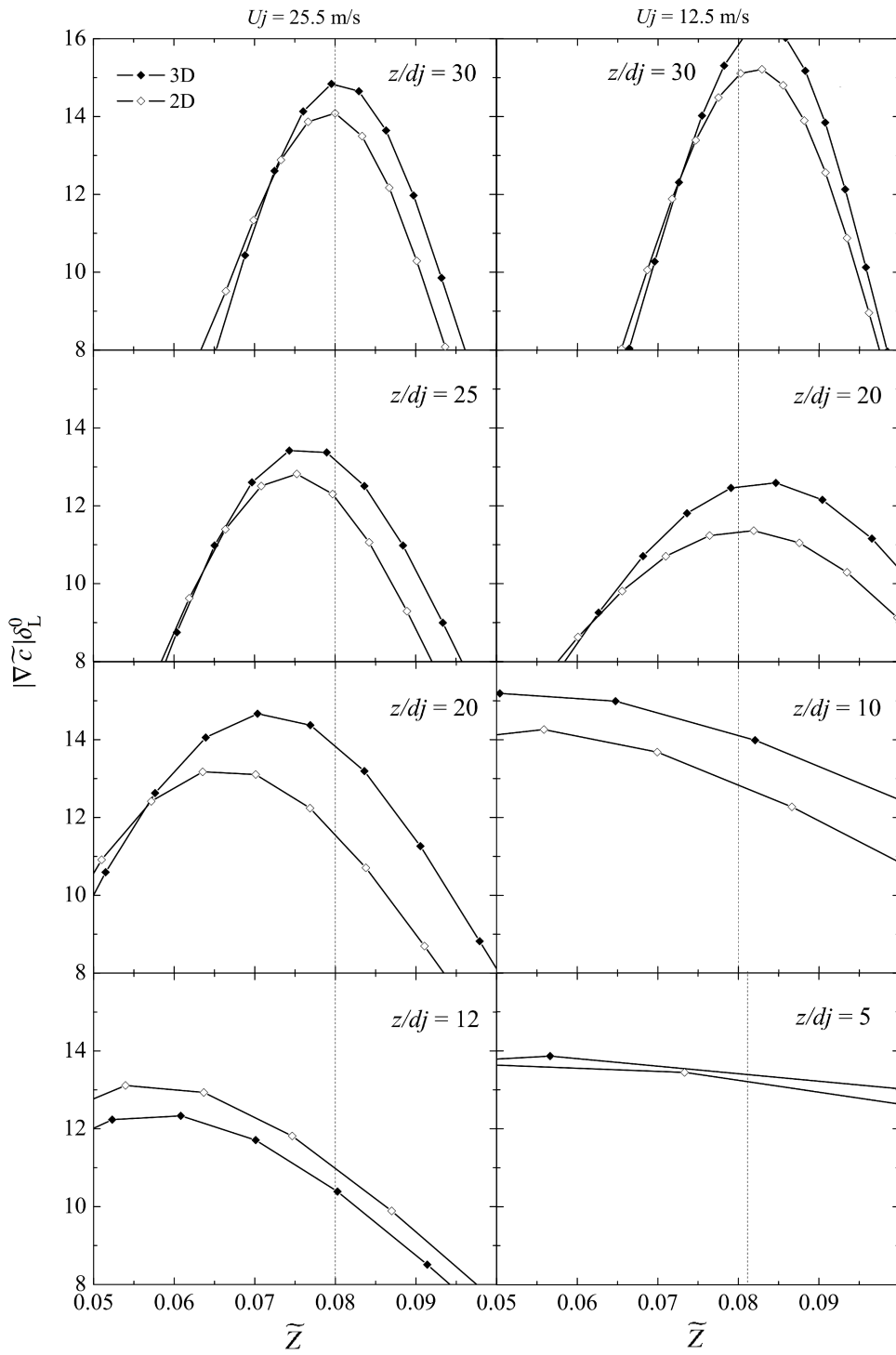
Figure 10.   Comparison of computed 2D (open symbol) and 3D (closed symbol) profiles of scaled progress variable gradient magnitude, $|\nabla \widetilde{c}|\delta_L^0$, in the mixture fraction space. δ_L^0 is the laminar flame thickness for stoichiometric methane-air mixture. The vertical dashed line corresponds to the flame most leading point marked in Figure 8d.